Article

The Impact of Topological States on the Thermoelectric Performance of p- and n-Type Sb_2Te_3/Bi_2Se_3-Multiwalled Carbon Nanotubes Heterostructured Networks

Jana Andzane [1], Krisjanis Buks [1,2], Elmars Spalva [2], Andrei Felsharuk [1] and Donats Erts [1,3,*]

[1] Institute of Chemical Physics, University of Latvia, Raina Blvd. 19, LV-1586 Riga, Latvia
[2] 3D Strong Ltd., Instituta Str. 36-17, LV-2130 Ulbroka, Latvia
[3] Faculty of Chemistry, University of Latvia, 1 Jelgavas Str., LV-1004 Riga, Latvia
* Correspondence: donats.erts@lu.lv

Abstract: The resistance and magnetoresistance of flexible thermoelectric p-type Sb_2Te_3-MWCNT, p-type Bi_2Se_3-MWCNT, and n-type Bi_2Se_3-MWCNT heterostructures were studied in the temperature range from 2 K to 300 K to reveal the conductance mechanisms governing the thermoelectric properties of these heterostructured networks. It was found that the conductance in heterostructured networks at different temperatures is governed by different processes and components of the networks. This effect was found to be related to the growth mechanisms of the Sb_2Te_3 and Bi_2Se_3 nanostructures on the MWCNT networks. At near-room temperatures, the Sb_2Te_3 and Bi_2Se_3 nanostructures were found to have the dominant contribution to the total conductance of the p-type Sb_2Te_3-MWCNT and n-type Bi_2Se_3-MWCNT networks. In turn, the conduction of p-type Bi_2Se_3-MWCNT heterostructured networks in a full temperature range and p-type Sb_2Te_3-MWCNT and n-type Bi_2Se_3-MWCNT heterostructured networks at temperatures below 30 K was governed by the MWCNTs; however, with the contribution from 2D topological states of Sb_2Te_3 and Bi_2Se_3 nanostructures, these were manifested by the weak antilocalization effect (WAL) cusps observed at temperatures below 5–10 K for all heterostructured networks considered in this work.

Keywords: topological insulator–carbon nanotube interface; heterostructured network; thermoelectric film; domestic waste heat conversion; magnetoresistance; bismuth and antimony chalcogenide

1. Introduction

In recent years, the study of nanostructured thermoelectric (TE) materials has become an emerging topic due to the increasing demand for energy-efficient processes and minimizing heat loss. TE material-based devices can transform waste heat into useful electrical energy and be used for thermal sensing [1]. The efficiency of TE materials is judged by the dimensionless figure of merit ZT, which is defined as $S^2 \cdot \sigma \cdot T \cdot \kappa^{-1}$, where S is the Seebeck coefficient of TE material, σ and κ are its electrical and thermal conductivities, respectively, and T is the absolute temperature. To increase the ZT of the material, it is necessary to increase σ and decrease κ; however, according to the Wiedemann–Franz law, the σ/κ ratio in bulk TE materials is restricted [2]. Bismuth and antimony chalcogenides (Bi_2Se_3, Bi_2Te_3, Sb_2Te_3, etc.) are widely known layered thermoelectric materials belonging to a class of 3D topological insulators (TI) [3–7]. Recently, it was predicted theoretically that downsizing these materials to the thickness of a few nm may form a hybridization gap between the top and bottom surface states of the material, resulting in the disengagement of σ and κ and a potentially significant increase in the existing ZT of the material [8,9]. At the same time, other theoretical works demonstrate that the parallel contribution of bulk and surface channels tend to cancel each other out, and the improvement of ZT in TIs with thicknesses below 10 nm is insignificant [10]. The experimental assay of these theoretical predictions performed for ultrathin Bi_2Se_3 and Sb_2Te_3 thin films were grown using the molecular beam

epitaxy (MBE) [10] or physical vapor deposition (PVD) [11] methods, yet did not show any significant improvement from the bulk values of ZT, which was attributed to the opposite contributions of the bulk and surface states of these materials. However, ultrathin (5–15 nm) the Bi_2Se_3 and (5–7 nm) Sb_2Te_3 films deposited by the PVD method showed thermoelectric properties comparable with thick MBE-grown thin films, presumably due to the quantum confinement effects originating from the downsizing and possible gapping of the topological surface states, and demonstrated their significant potential for their applications in TE generators (TEG) [11]. However, the main drawback to the application of Bi_2Se_3 and Sb_2Te_3 ultrathin films in TEGs is their fragility and the necessity to use solid substrates, which have relatively high thermal conductance. Recently, it was demonstrated by different research groups that combining bismuth and antimony chalcogenide nanostructures with carbon nanotubes (CNT) via the direct deposition of inorganic nanostructures on the CNT network via sputtering or PVD methods results in the formation of heterostructures which exhibit Seebeck coefficients comparable with that of bulk inorganic TE materials [12–16] and ZTs reaching 0.89 for some heterostructures, such as, for instance, Bi_2Te_3-CNT hybrid nanostructure scaffolds [12]. This high ZT value was attributed to the combination of the high electrical and low thermal conductivity of CNT networks [17] and the good room temperature thermoelectric properties of Bi_2Se_3, Bi_2Te_3, and Sb_2Te_3 [18,19]. The possibility of encapsulating such TI-CNT heterostructured networks in the non-conductive polymer without the significant degradation of thermoelectric properties and their high flexibility and mechanical and electrical stability under repetitive bending makes them attractive for use in wearable thermoelectric devices and other flexible electronic applications [20–22]. It was also shown that the PVD deposition of Bi_2Se_3 nanostructures on the MWCNT surface results in the formation of an up to 5 nm thin single-crystalline Bi_2Se_3 layer around the MWCNT, followed by the formation of free-standing Bi_2Se_3 nanoplates [16]. Thus, the good thermoelectric performance of bismuth chalcogenide-CNT heterostructures may also be the result of the contribution of topological surface states of Bi_2Te_3 or Bi_2Se_3 as was theoretically predicted. Potentially, dominating conductance mechanisms and the possible contribution of topological surface states to the properties of TI-CNT heterostructures may be revealed by analyzing the magnetoresistance measurements of the heterostructures. In recent years, topological insulator nanostructures have been found to exhibit magnetoresistance properties characterized by weak anti-localization (WAL) effects at temperatures below 30 K and low magnetic fields, which originate from the surface states of these materials [23–27]. In turn, the magnetoresistance of CNTs at low temperatures and low magnetic fields reveals the presence of weak localization (WL) effects [28–30]. The observation of WL and WAL effects in TI-CNT heterostructures, originating from the interface or interplay of the heterostructure components, may shed light on the dominating charge transfer processes occurring in these systems at different temperatures. For example, the presence of the WAL effect in Bi_2Se_3/Sb_2Te_3-MWCNT heterostructures indicates the suppression of bulk states due to the processes occurring at the interface between the TI and MWCNT and domination of the surface states in the TI material deposited on the MWCNTs. The hybridization of these surface states without compensating the contribution of bulk states could lead to a significant increase in the existing ZT of the bulk TI material [8,9]. This is interesting as thermoelectrics could open the path for the further employment of the hybridization effect of the topological surface states and for the improvement of properties of thermoelectric materials by combining them with CNTs, as well as many low-temperature spintronic applications [31,32], including magnetic sensors and memory devices [33,34], where magnetoresistance properties are crucial. However, to our knowledge, the systematic investigation of magnetoresistance in Bi_2Se_3/Sb_2Te_3-CNT heterostructures in the temperature range from 2 K to room temperature has not yet been performed.

In this work, the temperature dependencies of the resistance and magnetoresistance of p-type Sb_2Te_3-multiwalled carbon nanotubes (MWCNT) and p- and n-type Bi_2Se_3-MWCNT heterostructures were studied and analyzed to reveal the conductance mechanisms in these heterostructured networks. The results of this work provide insight into the potential use of

these heterostructured nanostructures in both thermoelectric and magnetoresistance-based applications.

2. Materials and Methods

2.1. Synthesis of MWCNTs

MWCNTs were synthesized using the chemical vapor deposition (CVD) method in a horizontal gas flow reactor. In this synthesis, ferrocene $Fe(C_5H_5)_2$ was used as a source for catalytic Fe nanoparticles. $Fe(C_5H_5)_2$ was dissolved in benzene at a concentration of 2 wt.%, and 100 mL of this solution was used for each synthesis cycle. An aerosol $Fe(C_5H_5)_2$ solution was then sprayed through a dispenser into the synthesis reactor at around 200 °C using argon as the carrier gas at a 20 mm/s flow rate. The total duration of the synthesis was 20 min. After cooling down the synthesis reactor, the MWCNTs were separated from the surface of the quartz tube of the reactor, yielding an MWCNT powder [35].

2.2. Synthesis of Sb_2Te_3/Bi_2Se_3-MWCNT Heterostructures

To obtain the Sb_2Te_3 or Bi_2Se_3 and MWCNT hybrid nanostructures, the MWCNTs' networks were first prepared on 25×25 mm^2 glass substrates using the spray-coating method—a 0.1 wt.% MWCNT suspension in isopropyl alcohol (IPA) was used for the spray-coating, resulting in MWCNT networks with a mass density of approximately 0.01 mg/cm^2. Afterwards, Bi_2Se_3 or Sb_2Te_3 nanostructures were deposited on the MWCNT networks using the catalyst-free physical vapor deposition method in a single-zone quartz furnace tube (GCL-1100X; MTI Corp., Richmond, CA, USA) equipped with a vacuum pump and nitrogen gas supply [16,36]. The Bi_2Se_3 or Sb_2Te_3 source material was placed in the center of the hot zone of the furnace at 585 °C, while the glass/MWCNT substrate was placed in the 470–390 °C zone. After this, the quartz furnace tube was flushed with nitrogen for 5 min, pumped down to a base pressure of 400 mTorr, and finally sealed. The synthesis was carried out by heating the quartz tube to a 585 °C temperature at a rate of 13 °C/min and then holding it at 585 °C for 15 min, after which the tube was left to cool naturally. As the tube cooled to 475 °C, it was filled with nitrogen and atmospheric pressure. The reference Sb_2Te_3 and Bi_2Se_3 nanostructured thin films were prepared using the same synthesis method with glass substrates. The thicknesses of the reference thin films were in the range of 200–400 nm. The amount of Bi_2Se_3 nanostructures deposited on the MWCNT networks varied depending on the amount of source material and the deposition duration. The wt.% of MWCNTs in Sb_2Te_3-MWCNT and Bi_2Se_3-MWCNT heterostructured networks was determined by weighing the substrate at each stage of preparation of the hybrid nanostructures (glass, bare MWCNT-coated glass, Sb_2Te_3/Bi_2Se_3-MWCNT coated glass) using an analytical balance (Precisa XR 205SM-DR, Dietikon, Switzerland).

2.3. The Morphology and Chemical Composition of the Samples

The morphology of the samples was characterized using a Hitachi S-4800 field-emission scanning electron microscope equipped with an energy-dispersive X-ray analyzer (123 eV; Bruker XFlash Quad 5040, Billerica, MA, USA). X-ray photoelectron spectroscopy measurements were carried out using a ThermoFisher ESCALAB Xi+ instrument with a monochromatic Al Kα X-ray source. The instrument-binding energy scale was calibrated to give a binding energy of 932.6 eV for the Cu $2p_{3/2}$ line of freshly etched metallic copper. The X-beam size used for the spectra recording was 900×10 μm with a pass energy of 20 eV and step size of 0.1 eV.

2.4. Room-Temperature Seebeck Coefficient Measurements

Room temperature Seebeck coefficient measurements were performed under ambient conditions using a laboratory-made device consisting of a Keithley 6430 Sub-Femtoamp remote source meter and an HP34401A digital multimeter; the device was calibrated using Standard Reference Material 3451 for the low-temperature Seebeck coefficient (NIST). For the Seebeck coefficient measurements, a two-part silver conductive epoxy (Agar scientific
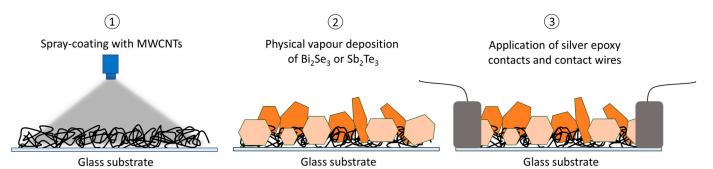
G3040, Stansted Mountfitchet, UK) was used to fabricate electrodes and to bond copper wires to each side of the hybrid network.

2.5. Magnetoresistance Measurements in the Temperature Range 2–300 K

Magnetoresistance (MR) is defined as MR = $(\rho(B) - \rho(0))/(\rho(0))$, where B is the magnetic field strength and $\rho(0)$ and $\rho(B)$ are the MWCNT film resistivities in the presence and absence of the magnetic field, respectively. For the determination of magnetoresistance, the resistances of the MWCNT networks were measured in a classic Hall bar configuration using the physical property measurement system (PPMS DynaCool-9T, Quantum Design, San Diego, CA, USA) at temperature and magnetic field strength in the range of 2 to 300 K and −9 T to +9 T, respectively. The samples were 10 mm × 10 mm in size; electrodes (70 nm Gold/5 nm Titanium) were applied using the thermal evaporation method (SIDRABE SAF EM sputtering vacuum system, Riga, Latvia). For the resistivity calculation, the thicknesses of the samples were measured using a profilometer Veeco Dektak 150.

3. Results and Discussion

Sb_2Te_3-MWCNT (with 6.5 wt.% of MWCNTs) and Bi_2Se_3-MWCNT (with 3 and 7.5 wt.% of MWCNTs) heterostructures were synthesized via the physical vapor deposition of Sb_2Te_3 or Bi_2Se_3 on pre-fabricated MWCNT networks, as shown in the schematics in Figure 1 and described elsewhere [16].

Figure 1. Schematics of the fabrication process of Bi_2Se_3/Sb_2Te_3-MWCNT heterostructured networks.

Deposited on the MWCNT network (Figure 2a), Bi_2Se_3 (Figure 2b), and Sb_2Te_3 (Figure 2c), nanostructures were represented mainly by randomly oriented nanoplate-like structures with thicknesses ~50–150 nm and ~300 nm, respectively.

While graphene substrates promote the epitaxial growth of Bi_2Se_3 and Sb_2Te_3 nanostructures due to the low lattice mismatch between graphene and Bi_2Se_3 or Sb_2Te_3 [37,38], a fundamental difference between the Bi_2Se_3-MWCNT and Sb_2Te_3-MWCNT heterostructures is found in the growth mechanism of the Bi_2Se_3 and Sb_2Te_3 nanostructures on the surfaces of curved nanotubes; while Bi_2Se_3 form shells around the individual MWCNTs, subsequently forming 15–30 nm thin nanoplates, the Sb_2Te_3 forms clusters of several hundred nanometers in size on energetically favorable locations, such as the junctions of nanotubes, without forming core–shell structures with the nanotubes, as described in detail in our previous work [16]. The chemical compositions of the synthesized MWCNT Sb_2Te_3 and Bi_2Se_3 nanostructures determined using EDX were 41 ± 3 at% Sb and 59 ± 3 at% Te and 42 ± 2 at% Bi and 58 ± 3 at% Se, respectively, which corresponds to stoichiometric Sb_2Te_3 and Bi_2Se_3. The chemical composition was confirmed using the XPS spectra recorded for the Bi_2Se_3 and Sb_2Te_3 nanostructured layers coating the MWCNTs in the Bi_2Se_3-MWCNT and Sb_2Te_3-MWCNT heterostructures. The deconvoluted high-resolution Bi 4f and Se 3d XPS spectra of the Bi_2Se_3 nanostructures revealed peaks located at 158.2 eV (Figure 2d), 53.8 eV, and 54.6 eV (Figure 2e), corresponding to Bi $4f_{7/2}$, Se $3d_{5/2}$ and Se $3d_{3/2}$, respectively, in the Bi_2Se_3 compound. The lower intensity peaks located at 158.9 eV (Figure 2d) and 54.8 eV (Figure 2e) correspond to the oxidized Bi_2Se_3, which is related to the presence of native oxide layer-coating Bi_2Se_3 nanostructures. The Bi:Se at.% profile recorded during

the etching of the surface of Bi_2Se_3 nanostructures confirmed their chemical composition as 42 ± 2 at% Bi and 58 ± 3 at% Se (Figure 2f). Peaks located at 530.2 eV (Figure 2g) and 573.6 eV (Figure 2h) correspond to Sb $3d_{5/2}$ and Te $3d_{5/2}$, respectively, in the Sb_2Te_3 compound. In turn, the peaks located at 531 eV (Figure 2g) and 576.8 eV (Figure 2h) correspond to the oxidized Sb_2Te_3. A relatively high intensity of these peaks is related to the susceptibility of the Sb_2Te_3 compound to rapid oxidation in air [39]. In addition, a peak located at 531.5 eV (Figure 2g) corresponds to the O1s signal, presumably originating from the hydroxyls of water adsorbed on the oxide layer in ambient conditions [40]. The Sb:Te at.% profile recorded during the etching of the surface of Sb_2Te_3 nanostructures confirmed their chemical composition at 41 ± 3 at% Bi and 58 ± 4 at% Te (Figure 2i) after the native oxide layer-coating Sb_2Te_3 nanostructures was etched off.
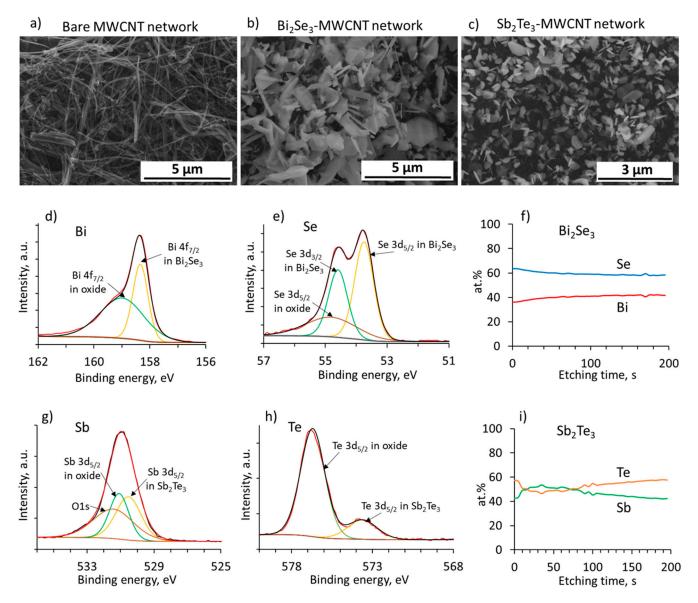

Figure 2. SEM images of (**a**) the bare MWCNT network, (**b**) the Bi_2Se_3-MWCNT heterostructured network, (**c**) Sb_2Te_3-MWCNT heterostructured network; (**d,e,g,h**) representative deconvoluted X-ray photoelectron spectroscopy (XPS) spectra of (**d,e**) Bi_2Se_3, and (**g,h**) Sb_2Te_3 nanostructured components of heterostructured networks (red and black curves represent respectively experimental data and fitting to the experimental data); and the (**f,i**) chemical composition of (**h**) Bi_2Se_3 and (**i**) Sb_2Te_3 nanostructures vs. etching time, recorded using XPS.

Based on previous research [16], MWCNT 6.5 wt.% in the Sb_2Te_3-MWCNT heterostructures was selected to obtain a Seebeck coefficient as high as possible while retaining the flexibility of the Sb_2Te_3-MWCNT network. In turn, in the case of Bi_2Se_3-MWCNT structures, MWCNT wt.% was chosen to obtain both negative and positive Seebeck coefficient values (Table 1). In the case of the deposition of Bi_2Se_3 (naturally n-type) on MWCNTs (naturally p-type), both components contributed to the Seebeck coefficient, tending to cancel each other. Thus, the Bi_2Se_3-MWCNT heterostructured networks with resulting n-type conductance can be obtained only at a low MWCNT wt.% in the heterostructures. In this case, the contribution of the established MWCNT Bi_2Se_3 network is dominant. The MWCNT wt.%-related transition from n-type to p-type conductance in these heterostructures is relatively rapid and occurs around the MWCNT content of 7–10 wt.% when the contribution of the MWCNTs to the Seebeck coefficient exceeds the contribution of Bi_2Se_3 [16].

Table 1. Seebeck coefficient values of different samples studied in this work.

Sample	Seebeck Coefficient, $\mu V \cdot K^{-1}$
Bare MWCNT network	$+16 \pm 5$
Sb_2Te_3-MWCNT network with MWCNT content 6.5 wt.%	$+74 \pm 7$
Bi_2Se_3-MWCNT network with MWCNT content 7.5 wt.%	$+11 \pm 3$
Bi_2Se_3-MWCNT network with MWCNT content three wt.%	-52 ± 5
Sb_2Te_3 thin film	$+85 \pm 8$
Bi_2Se_3 thin film	-100 ± 11

It can be seen from Table 1 that the bare MWCNT network had a p-type conductance and a Seebeck coefficient of ~+16 $\mu V \cdot K^{-1}$, which is a typical value for undoped MWCNTs [41]. Nanostructured Bi_2Se_3 and Sb_2Te_3 thin films, synthesized via the catalyst-free physical vapor deposition process, had Seebeck coefficients of ~-100 $\mu V \cdot K^{-1}$ and ~$+85$ $\mu V \cdot K^{-1}$, respectively, which are the values expected for these materials [16,36], and also indicate the type of conductance of these materials. The Seebeck coefficient value of ~+74 $\mu V \cdot K^{-1}$ obtained for Sb_2Te_3-MWCNT also correlates with previously reported data [16,42]. It indicates the dominant contribution of Sb_2Te_3 nanostructures to the total conductance of the Sb_2Te_3-MWCNT heterostructured network at room temperature. By contrast, Bi_2Se_3-MWCNT heterostructured networks showed Seebeck coefficients of ~+11 $\mu V \cdot K^{-1}$ for the network containing 7.5 wt.% of MWCNTs (referred to as p-type Bi_2Se_3-MWCNT further in the text) and ~-52 $\mu V \cdot K^{-1}$ for the network containing three wt.% of MWCNTs (referred to as n-type Bi_2Se_3-MWCNTs further in the text). These data indicate the presence of competing conduction mechanisms in the Bi_2Se_3-MWCNT heterostructures, both contributing to the total conductance.

To reveal the mechanisms governing the conduction in Sb_2Te_3-MWCNT and Bi_2Se_3-MWCNT-heterostructured networks, the resistance R and magnetoresistance MR of these samples were studied in the temperature region of 2–300 K. R(T) dependencies of bare MWCNT networks (Figure 3a) and reference nanostructured Sb_2Te_3 and Bi_2Se_3 thin films (Figure 3b,c) were shown to be typical for these materials' behavior [35,43–45]. The R(T) curve for the bare MWCNT network showed semiconductor behavior, where a monotonous incremental increase in the resistance with the decrease in the temperature from 300 K to ~30 K was followed by a rapid increase in resistance at temperatures below 30 K (Figure 3a).
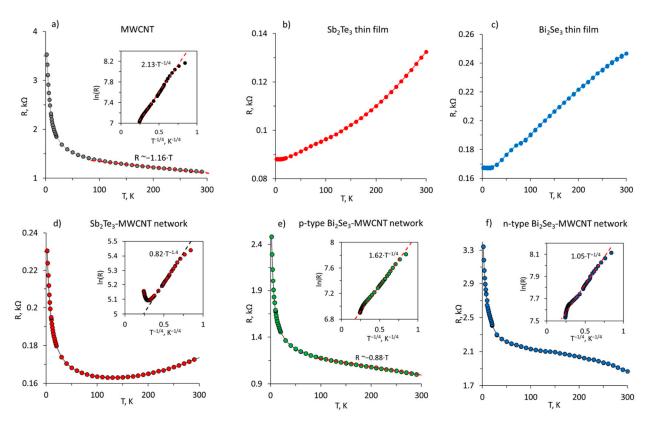
Figure 3. Temperature dependencies of resistance R of (**a**) the bare MWCNT network; (**b**) Sb_2Te_3 thin film; (**c**) Bi_2Se_3 thin film; (**d**) Sb_2Te_3-MWCNT heterostructured network; (**e**) p-type Bi_2Se_3-MWCNT heterostructured network; (**f**) and n-type Bi_2Se_3-MWCNT heterostructured network. Insets: ln(R) vs. $T^{1/4}$ plots (dashed curves represent fitting to the experimental data).

In the temperature region, 5–300 K, the R(T) curve of the bare MWCNT network (Figure 2a, inset) fitted well to the 3D Mott variable-range hopping (VRH) model for disordered systems [46–49], where conductance can be described by charge carrier hopping through localized states near the Fermi level and follows the formula $R = R_0 exp((T_0/T)^{1/4})$, where R_0 is a constant of proportionality representing the resistance of the sample at room temperature, and T_0 is Mott's characteristic temperature which is related to the energy required for the hopping of charge carriers and is determined as $T_0 = \beta/(k_B g(\mu)\alpha^3)$, where $\beta = 21$, k_B is the Boltzmann's constant, $g(\mu)$ is the density of states near the Fermi level and α is the localization length. At temperatures below 5 K, a deviation from Mott's law was observed due to Coulomb interactions between the localized electrons, which are not considered in Mott's model. In turn, as shown in Figure 3b,c, the R(T) curves of the nanostructured Sb_2Te_3 and Bi_2Se_3 thin films showed typical metallic behavior, expressed as a gradual decrease in the resistance with the decrease in temperature, which is in line with previous reports on the thin films of these materials [43,44]. However, the R(T) curve of the Sb_2Te_3-MWCNT heterostructured network showed a decrease in the resistance when the temperature decreased from 300 K to ~150 K, followed by its upturn at temperatures below 150 K with a rapid increase at temperatures below 30 K (Figure 3d). The U-turn shape of the R(T) curve of the Sb_2Te_3-MWCNT network indicates the temperature-dependent contribution of different mechanisms to the total conductance of this network. At temperatures between 5 and 150 K, the R(T) curve fits well with Mott's 3D VRH model (Figure 3d, inset), which indicates the domination of the hopping mechanism of conduction, which is typical for disordered CNT networks. At temperatures below 5 K, similar to that observed in the case of the bare MWCNT network, deviations from Mott's law, indicating Coulomb interactions between the localized electrons, were observed (Figure 3d, inset). However, the total resistance of the Sb_2Te_3-MWCNT heterostructured network was approximate. An order

of magnitude smaller than the resistance of the bare MWCNT network (Figure 3a) was comparable with the resistance values of the Sb_2Te_3 thin film (Figure 3b). Presumably, the decreased resistance in the temperature region 2–150 K was because of the effective charge transfer that occurred at the Sb_2Te_3–MWCNT interface and/or the increased mobility of the charge carriers due to the reduced Sb_2Te_3 interface barriers [50,51]. In the temperature region above 150 K, the Sb_2Te_3-MWCNT networks exhibit metallic behavior (Figure 3d), indicating the dominating contribution of interconnected Sb_2Te_3 nanostructures to the total conductance of the sample. The domination and the contribution of interconnected Sb_2Te_3 nanostructures to the total conductance of the Sb_2Te_3-MWCNT network is in line with the Seebeck coefficient of this network and is comparable with the Seebeck coefficient of the reference nanostructured Sb_2Te_3 thin film (74 $\mu V \cdot K^{-1}$ vs. 85 $\mu V \cdot K^{-1}$, Table 1). In addition, a significant difference was observed between the slopes of ln(R) vs. $T^{-1/4}$ curves of the bare MWCNT network (~2.13·$T^{-1/4}$, Figure 3a, inset) and Sb_2Te_3-MWCNT (~0.82·$T^{-1/4}$, Figure 3d, inset). Considering that the slopes of the ln(R) vs. $T^{-1/4}$ are related to Mott's characteristic temperature T_0, a possible reason for the lower slope of the ln(R) vs. $T^{-1/4}$ curve of Sb_2Te_3-MWCNT heterostructured networks in comparison with the slope of the bare MWCNT network is the increase in the localization length, and consequently, the increase in the charge carrier hopping distance and mobility [48,49].

In contrast with Sb_2Te_3-MWCNT, the R(T) curves of p-type and n-type Bi_2Se_3-MWCNT heterostructured networks (Figure 3e,f) showed a semiconductor behavior similar to bare MWCNT networks (Figure 3a). The R(T) curve of the p-type Bi_2Se_3-MWCNT network showed an incremental increase in the resistance with the decrease in temperature from 300 K down to ~30 K, followed by the rapid increase in the resistance at temperatures below 30 K (Figure 3e). At temperatures between 3 and 150 K, the R(T) curve fit Mott's 3D VRH model (Figure 3e, inset), which indicated the domination of the hopping mechanism of conduction similarly to disordered CNT networks [35,52–54]. The resistance values shown by the p-type Bi_2Se_3-MWCNT network were slightly lower in comparison with that of bare MWCNT networks, which could be related to the increase in localization length of the charge carriers due to the reduced potential barriers at MWCNT/Bi_2Se_3 interfaces similarly to the case of the Sb_2Te_3-MWCNT heterostructured network. This is supported by the lower value of the slope of the ln(R) vs. $T^{-1/4}$ curve of the p-type Bi_2Se_3-MWCNT network (Figure 3e) in comparison with that of the bare MWCNT network (1.62·$T^{-1/4}$ vs. 2.13·$T^{-1/4}$). In addition, there was a lower slope of the R(T) curve for the p-type Bi_2Se_3-MWCNT heterostructured network in the temperature range 100–300 K (~−0.88·T, Figure 3e) in comparison with that of the bare MWCNT network (~−1.16·T, Figure 3a), which may indicate the contribution of the metallic conductance of interconnected Bi_2Se_3 nanostructures to the total conductance of the p-type Bi_2Se_3-MWCNT network. This presumption is supported by the Seebeck coefficient values of the p-type Bi_2Se_3-MWCNT heterostructured network, which are lower by ~30% than the Seebeck coefficient values of bare MWCNT networks (Table 1). However, the positive values of the Seebeck coefficient or p-type Bi_2Se_3-MWCNT networks indicate that the contribution of Bi_2Se_3 to the total conductance, in this case, is not dominating. In turn, R(T) curve of the n-type Bi_2Se_3-MWCNT heterostructured network showed a nonlinear incremental increase in R with a temperature decrease from 300 K down to 100 K (Figure 3f), indicating the presence of two competing temperature-dependent mechanisms of conductance, followed by the rapid increase in R in the temperature region below 30 K (Figure 3f), which was similar to that shown by the bare MWCNT network (Figure 3a). Noticeable deviations in the R(T) curve from Mott's 3D VRH model in the temperature region above 30 K (Figure 3f, inset) suggest the contribution of the metallic conductance mechanism and phonon-assisted conduction processes to the total conductance of the n-type Bi_2Se_3-MWCNT heterostructured network. The slope of the ln(R) vs. $T^{-1/4}$ curve is lower in comparison with that of p-type Bi_2Se_3-MWCNT heterostructured networks (~1.05·$T^{-1/4}$ vs. 1.62·$T^{-1/4}$, Figure 3e,f), which may point to the further increase in the localization length in comparison with p-type Bi_2Se_3-MWCNT networks. However, the resistance of the n-type Bi_2Se_3-MWCNT network is

higher than that of the p-type Bi_2Se_3-MWCNT network and comparable with the resistance of the bare MWCNT network. Considering the negative Seebeck coefficient values of the n-type Bi_2Se_3-MWCNT heterostructured networks (~ -52 μV·K^{-1}, Table 1), presumably, the dominating conduction path in the case of n-type Bi_2Se_3-MWCNT heterostructured networks is through the thin Bi_2Se_3 layers formed on the surfaces of MWCNTs. As was reported previously, the direct physical vapor deposition of Bi_2Se_3 on the surfaces of MWCNTs resulted in the formation of an up to 5 nm thin Bi_2Se_3 layer around the MWCNT, followed by the growth of free-standing Bi_2Se_3 nanostructures [16]. Presumably, in p-type Bi_2Se_3-MWCNT networks, the contribution of Bi_2Se_3 to the total conductance comes from the interconnected free-standing Bi_2Se_3 nanoplates, while thin Bi_2Se_3 layers grown on the surfaces of MWCNTs do not form a well-interconnected network. However, in the n-type Bi_2Se_3-MWCNT network, the Bi_2Se_3 thin layers formed on the surfaces of MWCNTs may be interconnected. Previously, it has been shown by other research groups that the deposition of Bi_2Se_3 on graphene results in the formation of a separate n-type conductive channel in the Bi_2Se_3-graphene system if the Bi_2Se_3 thickness is <8 nm [55]. In addition, it was shown by our research group that in contrast to the behavior of Bi_2Se_3-nanostructured thin films with thicknesses above 10 nm, showing the metallic type of conductance, Bi_2Se_3 thin films with thicknesses below 6 nm show a semiconductor type of conductance, expressed as an increase in the resistance with a decrease in temperature [11]. In addition, the Seebeck coefficient shown by ~5 nm thin Bi_2Se_3 films was ~ -40 μV·K^{-1} [11], which is comparable with the Seebeck coefficient shown by the n-type Bi_2Se_3-MWCNT network (~ -52 μV·K^{-1}, Table 1).

Magnetoresistance measurements confirmed the different mechanisms of the total conductance of Sb_2Te_3-MWCNT and Bi_2Se_3-MWCNT heterostructured networks. The magnetoresistance of bare MWCNT networks was found to be negative in all ranges of magnetic fields and temperatures and to increase with the decrease in temperature, reaching $\sim -10\%$ at a temperature of 2 K and magnetic field B of ± 9 T (Figure 4a). Such magnetoresistance behavior is typical for p-type MWCNTs. Generally, it is explained by the relative changes in conductivity due to the effects of weak localization and charge carriers' interaction, which are both proportional to the temperature [35,53].

In contrast, the magnetoresistance of Sb_2Te_3 (Figure 4b) and Bi_2Se_3 (Figure 4c) nanostructured films were found to be positive in all ranges of temperatures and magnetic fields, reaching ~10% for Sb_2Te_3 nanostructured films and ~30% for Bi_2Se_3 nanostructured films at a temperature of 2–30 K and B $\pm$ 9T. Positive magnetoresistance is typical for the Sb_2Te_3 and Bi_2Se_3 with the metallic type of conductance [23,43,56,57]. It is generally explained as caused by the Lorentz force deflecting the charge carriers from the initial path to cyclotron orbiting. Both Sb_2Te_3 and Bi_2Se_3 exhibit B^2 dependence of the magnetoresistance (Figure 4b,c), which is characteristic of the dominating bulk transport [23]. Positive magnetoresistance decreases with the increase in temperature due to the suppression of mobility in the charge carriers because of phonon-assisted charge carrier scattering. No weak antilocalization effect was observed for the Sb_2Te_3 thin film (Figure 4b, inset), presumably due to the significant thickness of the Sb_2Te_3 thin film, resulting in the presence of dominant bulk charge carriers, masking the effects arising from topologically protected surface states. In contrast, despite the B^2 dependence of magnetoresistance, indicating the domination of bulk charge carriers, the Bi_2Se_3 thin film exhibited a slight WAL at temperatures below 10 K (Figure 4c, inset). Typically, WAL is observed in Bi_2Se_3 thin films with thicknesses of <100 nm [23]. The weak WAL effect in thicker Bi_2Se_3 nanostructured film could be related to the fact that this film is nanostructured and consists of randomly oriented nanoplates [58].
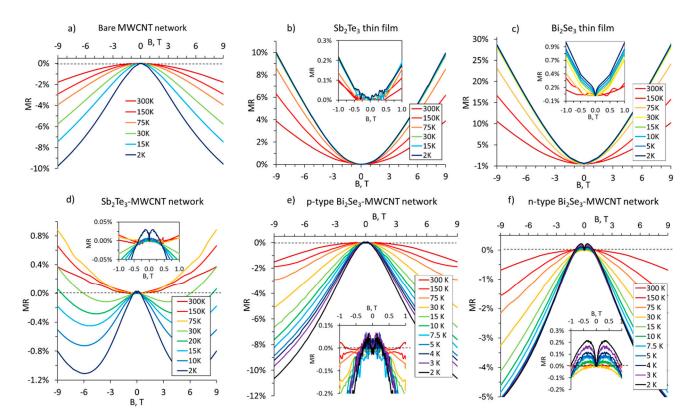
Figure 4. Magnetoresistance at different temperatures of (**a**) the bare MWCNT network; (**b**) Sb_2Te_3 nanostructured thin film; (**c**) Bi_2Se_3 nanostructured thin film; (**d**) the Sb_2Te_3-MWCNT heterostructured network; (**e**) p-type Bi_2Se_3-MWCNT heterostructured network; (**f**) and n-type Bi_2Se_3-MWCNT heterostructured network. Insets: a close look at magnetoresistance curves at low magnetic fields.

Despite both components of Sb_2Te_3-MWCNT heterostructured networks being naturally p-type, their magnetoresistance (Figure 4d) indicates the presence of different competing temperature-dependent mechanisms of conductance observed previously in the R vs. T behavior of the samples. At temperatures above 75 K, the magnetoresistance of the Sb_2Te_3-MWCNT heterostructured networks is positive and follows the tendency of the magnetoresistance of the Sb_2Te_3 thin film (Figure 4b), which most likely points to the dominant contribution of Sb_2Te_3 nanostructures to the conductance of the sample. However, the magnitude of the positive magnetoresistance of the MWCNT-Sb_2Te_3 hybrid network is by an order of magnitude smaller in comparison with that of the Sb_2Te_3 thin film, and presumably due to the competing effect of the negative magnetoresistance of MWCNTs. At temperatures of 30 K and below, the magnetoresistance becomes negative and increases with the temperature decrease at low magnetic fields. However, it exhibits a U-turn to positive values at high magnetic fields (Figure 4d). Presumably, the dominant contribution to the magnetoresistance comes from the MWCNTs at low magnetic fields and low temperatures. However, at higher magnetic fields, the contribution of the positive magnetoresistance of the Sb_2Te_3 network, arising from the impact of the Lorentz force, becomes significant and results in a U-turn in the total magnetoresistance (Figure 4d). The absolute values of negative magnetoresistance of Sb_2Te_3-MWCNT networks are also by an approximate order of magnitude more minor in comparison with the magnetoresistance of bare MWCNTs, which proves the competing of two conductance mechanisms. It should be noted that in the Sb_2Te_3-MWCNT, a weak antilocalization (WAL) effect with a magnitude of ~0.03% was observed at 2 K (Figure 4f, inset). Typically, the WAL effect of an order of magnitude higher value is observed for the Sb_2Te_3 flakes of thicknesses ~25 nm [43]. The appearance of the WAL in the magnetoresistance curves of Sb_2Te_3-MWCNT networks may be related to the tuning of the Fermi level of Sb_2Te_3 as a result of the charge transfer at

the Sb_2Te_3 interface, resulting in the ability to observe topological properties of the Sb_2Te_3 nanostructures [59].

In contrast to the Sb_2Te_3-MWCNT heterostructured networks, both p-type and n-type Bi_2Se_3-MWCNT heterostructured networks (Figure 4e,d) exhibited negative magnetoresistance in the entire temperature range from 2 K to 300 K at magnetic fields higher than ±0.5 T, reaching ~−10% and ~−5%, respectively, at the maximal magnetic field of ±9 T. Presumably, the negative magnetoresistance of the p-type Bi_2Se_3-MWCNT heterostructured network, which is similar to the magnetoresistance of the bare MWCNT network (Figure 4a,e), indicates the dominating role of MWCNTs in the conductance of this heterostructured network with a minor contribution from the Bi_2Se_3 nanostructured network. In turn, the negative magnetoresistance of n-type Bi_2Se_3-MWCNT (Figure 4f) is ~50% lower in comparison with the magnetoresistance of the p-type Bi_2Se_3-MWCNT heterostructured network (Figure 4e) and bare MWCNT network (Figure 4a). This may indicate the influence of MWCNTs' contribution of Bi_2Se_3 nanostructures in the total conductance of this sample, which is significantly more pronounced in comparison with the p-type Bi_2Se_3-MWCNT heterostructured networks and may arise from the interconnected few nm thin Bi_2Se_3 layers coating the surfaces of MWCNTs [16]. The contribution of the Bi_2Se_3 nanostructures to the total conductance of Bi_2Se_3-MWCNT heterostructured samples is also indicated by WAL cusps, which were observable for both p-type and n-type Bi_2Se_3-MWCNT heterostructured networks at low temperatures and magnetic fields lower than ±0.5 T (Figure 4e,f, insets) and were typically observed for Bi_2Se_3 nanostructures and thin films. For the p-type Bi_2Se_3-MWCNT, the WAL cusps were less pronounced and observed at temperatures below 5 K (Figure 4e, inset). In turn, for the n-type Bi_2Se_3-MWCNT heterostructured networks, the WAL cusps had ~three times higher intensity (Figure 4f, inset) and were detectable at higher temperatures compared with the p-type Bi_2Se_3-MWCNT (≤10 K vs. ≤5 K for n-type and p-type Bi_2Se_3-MWCNT networks, respectively). Data on the magnetoresistance of different samples at 2 K are summarized in Table 2.

Table 2. Magnetoresistance of MWCNTs, Bi_2Se_3/Sb_2Te_3 thin films, Bi_2Se_3-MWCNT and Sb_2Te_3-MWCNT heterostructured networks at 2 K.

Sample	MR, %	WAL	Comment
MWCNT networks, this work	−10	no	
MWCNTs/polyvinyl acetate [53]	−3	no	Low magnetoresistance may be related to the impact of the binder
Sb2Te3, this work	+10	no	
Sb2Te3, PVD grown [43]	+50 +100	yes/no	0.25% WAL observed only for the 25 nm thin flake.
Bi2Se3, this work	+30	yes	
Bi2Se3, MBE grown [23]	+5	yes	For thicknesses < 100 nm
Sb2Te3-MWCNT, this work	−1.1	yes	MR upturn at high (>6 T) magnetic fields
p-type Bi2Se3-MWCNT, this work	−11	yes	WAL + 0.03%
n-type Bi2Se3-MWCNT, this work	−5	yes	WAL + 0.2%

Phase coherence lengths estimated from the Hikami–Larkin–Nagaoka (HLN) equation's fit (Figure 5a) for magnetoconductance [60]:

$$\Delta G(B) = -\alpha \frac{e^2}{\pi h}\left[\psi\left(\frac{1}{2} + \frac{\hbar}{4el_\phi^2 B}\right) - ln\left(\frac{\hbar}{4el_\phi^2 B}\right)\right]$$

where ψ is the digamma function, α is a prefactor depending on the contribution of competing conduction channels, and l_ϕ is the phase coherence length, which exhibited a power

law behavior for both p-type and n-type Bi_2Se_3-MWCNT networks with the relationships $l_\phi \sim T^{-0.46}$ and $l_\phi \sim T^{-0.59}$ (Figure 5b), which are close to the theoretical power law dependence of $l_\phi \sim T^{-1/2}$ for 2D topological insulator systems [27]. This indirectly proves that the WAL at low magnetic fields may originate from the 2D surface states of Bi_2Se_3 nanostructures.
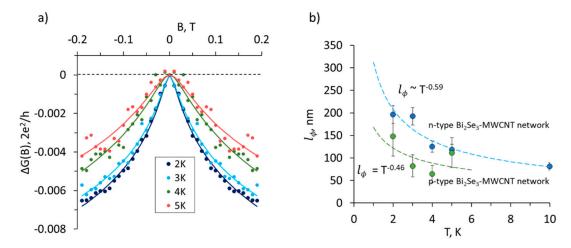

Figure 5. (**a**) The change in magnetoconductance of the n-type Bi_2Se_3-MWCNT heterostructured network, which fits the HLN theory for the temperatures 2–5 K; (**b**) the temperature dependence of the phase coherence length l_ϕ of p-type and n-type Bi_2Se_3-MWCNT heterostructured networks.

The range of temperature-dependent l_ϕ was 60–150 nm for p-type Bi_2Se_3 MWCNT networks and 80–200 nm for n-type Bi_2Se_3-MWCNT networks, which is in line with the l_ϕ values reported for the Bi_2Se_3 nanostructures ($l_\phi \sim$100–200 nm) [61]. Higher l_ϕ values of the n-type Bi_2Se_3-MWCNT network in comparison to those of the p-type Bi_2Se_3-MWCNT network could be related to the higher amount of Bi_2Se_3 in the n-type network, resulting in an increase in the interconnections between the Bi_2Se_3 nanostructures and the formation of larger Bi_2Se_3 clusters.

The determined negative values of prefactor α varied from -0.02 to -0.1 for the p-type Bi_2Se_3-MWCNT network and around -0.02 for the n-type Bi_2Se_3-MWCNT network (Table 3), which is significantly smaller than the typical α values, ranging from -0.5 to -1.5 and suggesting single ($\alpha = -0.5$) or multiple ($\alpha = -1; -1.5$) independent bands with WAL [62].

Table 3. Phase coherence length l_ϕ and prefactor α determined using the Hikami–Larkin–Nagaoka theory for p-type and n-type Bi2Se3-MWCNT networks for the 2–10 K temperature range.

T, K	p-Type Bi_2Se_3-MWCNT Network		n-Type Bi_2Se_3-MWCNT Network	
	l_ϕ, nm	α	l_ϕ, nm	α
2	148	−0.02	197	−0.02
3	82	−0.1	192	−0.021
4	64	−0.1	125	−0.025
5	111	−0.02	118	−0.024
10	-		82	−0.023

Presumably, close-to-zero values of prefactor α may indicate the contribution of both weak localization (WL), originating from MWCNTs [28–30], and WAL, originating from Bi_2Se_3 nanostructures. It was shown previously that the WL and WAL may coexist in the quantum diffusion regime in systems where the mean free path of the charge carrier due to elastic scattering is much shorter than the sample size, but the phase coherence length l_ϕ due to inelastic scattering is comparable with the sample size. The transition from WAL to WL corresponds to the change in prefactor α in the HLN formula from a negative to a

positive value [62]. In addition, the thickness-dependent transition of WAL to WL was also previously observed for Bi_2Se_3 films grown via PVD on graphene substrates and explained by the dependence of the band bending of Bi_2Se_3/graphene and Bi_2Se_3/air interfaces on the thickness of the Bi_2Se_3 film [63]. It should be noted that, as revealed in the Sb_2Te_3-MWCNT and Bi_2Se_3-MWCNT heterostructured networks, the contribution of 2D topological states of the Sb_2Te_3 and Bi_2Se_3 expressed by the appearance of WAL at low temperatures may open the path for the further enhancement of the thermoelectrical properties of such networks via the optimization of the geometry (in particular, the thickness) of the deposited nanostructures, as well as the TI:MWCNT mass ratio [7,64].

4. Conclusions

The resistance and magnetoresistance of thermoelectric p-type Sb_2Te_3-MWCNT (S~74 $\mu V \cdot K^{-1}$), p-type Bi_2Se_3-MWCNT (S~11 $\mu V \cdot K^{-1}$), and n-type Bi_2Se_3-MWCNT (S~-52 $\mu V \cdot K^{-1}$) heterostructured networks prepared via the direct physical vapor deposition of Sb_2Te_3 and Bi_2Se_3 nanostructures on MWCNT networks were measured in the 2 K to 300 K temperature range and compared with the properties of bare MWCNT networks (S~16 $\mu V \cdot K^{-1}$) and the reference Sb_2Te_3 and Bi_2Se_3 nanostructured thin films revealed the conductance governing mechanisms in these heterostructured networks and their contribution to the thermoelectric properties. It was found that in the Sb_2Te_3-MWCNT and Bi_2Se_3-MWCNT heterostructured networks, the conductance at different temperatures is governed by different mechanisms and different components of this network. In Sb_2Te_3-MWCNT networks, the conductance at temperatures ranging from 150 K to 300 K temperatures is dominated by the Sb_2Te_3 nanostructures, resulting in a high Seebeck coefficient of the Sb_2Te_3-MWCNT network and lower in comparison to the bare MWCNT network resistance, which may be favorable for the applications of Sb_2Te_3-MWCNT networks in flexible thermoelectrics. Below 150 K, the resistance curve showed a gradual upturn, indicating the decreasing contribution of Sb_2Te_3 to the conduction. At temperatures below 30 K, the conductance in these heterostructured networks is mainly governed by the MWCNT network except at the lowest measurement temperature of 2 K, where a low-intensity WAL cusp was observed, indicating the possible minor contribution of the surface states of Sb_2Te_3 to the conduction. In contrast, the conductance mechanisms in p-type and n-type Bi_2Se_3-MWCNT heterostructured networks were found to be more sophisticated. In these networks, the amount of the deposited Bi_2Se_3 material determined the magnitude of its contribution to the total conductance. It was found that in p-type Bi_2Se_3-MWCNT heterostructured networks, the dominant contributor to the conductance of the network in the entire temperature range from 2 K to 300 K were MWCNTs with a minor contribution from Bi_2Se_3 nanostructures, expressed in the lower by the ~30% Seebeck coefficient in comparison to the bare MWCNT networks and appearance of low-intensity WAL cusps in the magnetoresistance curves measured at temperatures below 5 K, indicating the contribution of the 2D surface states of Bi_2Se_3. By contrast, in the n-type Bi_2Se_3-MWCNT heterostructured network, which was prepared using a higher amount of Bi_2Se_3, the total conductance is the result of the competing contributions of the MWCNT network and Bi_2Se_3 nanostructured network, leading to the significant negative Seebeck coefficient accompanied by the increased resistance of the heterostructured network. The magnitude of WAL observed in the magnetoresistance curves of the n-type Bi_2Se_3-MWCNT heterostructured networks was significantly higher in comparison with the other heterostructures studied in this work and was observed at higher temperatures (below 10 K). Presumably, the difference between the p-type and n-type Bi_2Se_3-MWCNT heterostructured networks is in the type of contribution made by the Bi_2Se_3 nanostructures. In the p-type Bi_2Se_3-MWCNT networks, the Bi_2Se_3 contribution may arise from the network of interconnected free-standing Bi_2Se_3 nanostructures. In contrast, in the n-type Bi_2Se_3-MWCNT networks, this contribution may come from the interconnected few nm thin layers of Bi_2Se_3 surrounding the MWCNTs. In the latter case, separate n-type conductive channels may be formed at the MWCNT/Bi_2Se_3 interface, which leads to the n-type conductance of

this network. The fitting of the low-temperature magnetoconductance of the p-type and n-type Bi_2Se_3-MWCNT heterostructured networks to the Hikami–Larkin–Nagaoka (HLN) theory confirmed the contribution of the 2D surface states, originating from the Bi_2Se_3 component of the heterostructured networks. In addition, the fit to the HLN indicated the possible co-existence of WAL and WL in these heterostructures, which may originate from Bi_2Se_3 nanostructures and MWCNTs, respectively. These findings open the path for further research and the optimization of TI-CNT heterostructures for application in flexible thermoelectrics and, as revealed in this work, the contribution of topological states to their conducting mechanisms may significantly improve the thermoelectrical properties of the heterostructured networks.

Author Contributions: Conceptualization, D.E.; methodology, J.A., K.B. and D.E.; investigation, K.B., J.A., E.S. and A.F.; Visualization, K.B. and E.S.; writing—original draft preparation K.B. and J.A. with the contributions from all authors; writing—review and editing, D.E.; supervision, D.E. All authors have read and agreed to the published version of the manuscript.

Institutional Review Board Statement: Not applicable.

Informed Consent Statement: Not applicable.

Data Availability Statement: Data are contained within the article.

Conflicts of Interest: Authors Krisjanis Buks and Elmars Spalva were employed by the company 3D Strong Ltd. The remaining authors declare that the research was conducted in the absence of any commercial or financial relationships that could be construed as a potential conflict of interest.

References

1. He, R.; Schierning, G.; Nielsch, K. Thermoelectric Devices: A Review of Devices, Architectures, and Contact Optimization. *Adv. Mater. Technol.* **2018**, *3*, 1700256. [CrossRef]
2. Yadav, A.; Deshmukh, P.C.; Roberts, K.; Jisrawi, N.M.; Valluri, S.R. An analytic study of the Wiedemann–Franz law and the thermoelectric figure of merit. *J. Phys. Commun.* **2019**, *3*, 105001. [CrossRef]
3. Fang, L.; Jia, Y.; Miller, D.J.; Latimer, M.L.; Xiao, Z.L.; Welp, U.; Crabtree, G.W.; Kwok, W.K. Catalyst-free growth of millimeter-long topological insulator Bi_2Se_3 nanoribbons and the observation of the π-berry phase. *Nano Lett.* **2012**, *12*, 6164–6169. [CrossRef]
4. Kim, D.; Syers, P.; Butch, N.P.; Paglione, J.; Fuhrer, M.S. Ambipolar surface state thermoelectric power of topological insulator Bi2Se3. *Nano Lett.* **2014**, *14*, 1701–1706. [CrossRef] [PubMed]
5. Kumar, A.; Cecchini, R.; Locatelli, L.; Wiemer, C.; Martella, C.; Nasi, L.; Lazzarini, L.; Mantovan, R.; Longo, M. Large-Area MOVPE Growth of Topological Insulator Bi_2Te_3 Epitaxial Layers on i-Si(111). *Cryst. Growth Des.* **2021**, *21*, 4023–4029. [CrossRef]
6. Sung, J.H.; Heo, H.; Hwang, I.; Lim, M.; Lee, D.; Kang, K.; Choi, H.C.; Park, J.H.; Jhi, S.H.; Jo, M.H. Atomic layer-by-layer thermoelectric conversion in topological insulator bismuth/antimony tellurides. *Nano Lett.* **2014**, *14*, 4030–4035. [CrossRef]
7. Chudzinski, P. Contribution of 1D topological states to the extraordinary thermoelectric properties of Bi_2Te_3. *Proc. R. Soc. A Math. Phys. Eng. Sci.* **2020**, *476*, 20200088. [CrossRef]
8. Ghaemi, P.; Mong, R.S.K.; Moore, J.E. In-plane transport and enhanced thermoelectric performance in thin films of the topological insulators Bi_2Te_3 and Bi_2Se_3. *Phys. Rev. Lett.* **2010**, *105*, 166603. [CrossRef]
9. Tahir, M.; Manchon, A.; Schwingenschlögl, U. Enhanced thermoelectric power in ultrathin topological insulators with magnetic doping. *J. Appl. Phys.* **2014**, *116*, 093708. [CrossRef]
10. Guo, M.; Wang, Z.; Xu, Y.; Huang, H.; Zang, Y.; Liu, C.; Duan, W.; Gan, Z.; Zhang, S.C.; He, K.; et al. Tuning thermoelectricity in a Bi_2Se_3 topological insulator via varied film thickness. *New J. Phys.* **2016**, *18*, 015008. [CrossRef]
11. Andzane, J.; Felsharuk, A.; Sarakovskis, A.; Malinovskis, U.; Kauranens, E.; Bechelany, M.; Niherysh, K.A.; Komissarov, I.V.; Erts, D. Thickness-dependent properties of ultrathin bismuth and antimony chalcogenide films formed by physical vapor deposition and their application in thermoelectric generators. *Mater. Today Energy* **2021**, *19*, 100587. [CrossRef]
12. Jin, Q.; Jiang, S.; Zhao, Y.; Wang, D.; Qiu, J.; Tang, D.M.; Tan, J.; Sun, D.M.; Hou, P.X.; Chen, X.Q.; et al. Flexible layer-structured Bi_2Te_3 thermoelectric on a carbon nanotube scaffold. *Nat. Mater.* **2019**, *18*, 62–68. [CrossRef] [PubMed]
13. Zhao, Y.; Li, Y.; Qiao, J.; Jiang, S.; Mao, P.; Qiu, J.; Kang, S.; Tan, J.; Tai, K.; Liu, C. Decoupling phonon and carrier scattering at carbon nanotube/Bi_2Te_3 interfaces for improved thermoelectric performance. *Carbon N. Y.* **2020**, *170*, 191–198. [CrossRef]

14. Li, Y.; Zhao, Y.; Qiao, J.; Jiang, S.; Qiu, J.; Tan, J.; Zhang, L.; Gai, Z.; Tai, K.; Liu, C. A Flexible and Infrared-Transparent Bi$_2$Te$_3$-Carbon Nanotube Thermoelectric Hybrid for both Active and Passive Cooling. *ACS Appl. Electron. Mater.* **2020**, *2*, 3008–3016. [CrossRef]

15. Tseng, S.C.; Wang, C.A.; Chu, H.S.; Tsai, H.Y. Thermoelectric properties of a vertically aligned carbon nanotube array with embedded bismuth telluride. *J. Mater. Sci.* **2022**, *57*, 19396–19404. [CrossRef]

16. Buks, K.; Andzane, J.; Smits, K.; Zicans, J.; Bitenieks, J.; Zarins, A.; Erts, D. Growth mechanisms and related thermoelectric properties of innovative hybrid networks fabricated by direct deposition of Bi$_2$Se$_3$ and Sb$_2$Te$_3$ on multiwalled carbon nanotubes. *Mater. Today Energy* **2020**, *18*, 100526. [CrossRef]

17. Kumanek, B.; Janas, D. Thermal conductivity of carbon nanotube networks: A review. *J. Mater. Sci.* **2019**, *54*, 7397–7427. [CrossRef]

18. Kulbachinskii, V.A.; Kytin, V.G.; Kudryashov, A.A.; Tarasov, P.M. Thermoelectric properties of Bi$_2$Te$_3$, Sb$_2$Te$_3$ and Bi$_2$Se$_3$ single crystals with magnetic impurities. *J. Solid State Chem.* **2012**, *193*, 47–52. [CrossRef]

19. Osterhage, H.; Gooth, J.; Hamdou, B.; Gwozdz, P.; Zierold, R.; Nielsch, K. Thermoelectric properties of topological insulator Bi$_2$Te$_3$, Sb$_2$Te$_3$, and Bi$_2$Se$_3$ thin film quantum wells. *Appl. Phys. Lett.* **2014**, *105*, 123117. [CrossRef]

20. Andzane, J.; Buks, K.; Bitenieks, J.; Bugovecka, L.; Kons, A.; Merijs-meri, R.; Svirksts, J.; Zicans, J.; Erts, D. p-Type PVA/MWCNT-Sb$_2$Te$_3$ Composites for Application in Different Types of Flexible Thermoelectric Generators in Combination with n-Type PVA/MWCNT-Bi2Se3 Composites. *Polymers* **2022**, *14*, 5130. [CrossRef]

21. Buks, K.; Andzane, J.; Bugovecka, L.; Katkov, M.V.; Smits, K.; Starkova, O.; Katkevics, J.; Bērziņš, A.; Brauna, L.; Voikiva, V.; et al. Highly Efficient Flexible n-Type Thermoelectric Films Formed by Encapsulation of Bi$_2$Se$_3$-MWCNT Hybrid Networks in Polyvinyl Alcohol. *Adv. Mater. Interfaces* **2022**, *9*, 2200318. [CrossRef]

22. Bugovecka, L.; Buks, K.; Andzane, J.; Miezubrale, A.D.; Bitenieks, J.; Zicans, J.; Erts, D. Positive and Negative Changes in the Electrical Conductance Related to Hybrid Filler Distribution Gradient in Composite Flexible Thermoelectric Films Subjected to Bending. *Nanomaterials* **2023**, *13*, 1212. [CrossRef] [PubMed]

23. Gracia-Abad, R.; Sangiao, S.; Bigi, C.; Chaluvadi, S.K.; Orgiani, P.; De Teresa, J.M. Omnipresence of weak antilocalization (WAL) in Bi$_2$Se$_3$ thin films: A review on its origin. *Nanomaterials* **2021**, *11*, 1077. [CrossRef] [PubMed]

24. Kuzanyan, A.A.; Harutyunyan, S.R. Weak Localization and Weak Anti-Localization in Ultra Thin Sb$_2$Te$_3$ Nanoplates. *J. Contemp. Phys.* **2021**, *56*, 359–365. [CrossRef]

25. Ding, D.; Dai, X.; Wang, C.; Diao, D. Temperature dependent crossover between positive and negative magnetoresistance in graphene nanocrystallines embedded carbon film. *Carbon N. Y.* **2020**, *163*, 19–25. [CrossRef]

26. Garg, R.; Gopalan, D.P.; De La Barrera, S.C.; Hafiz, H.; Nuhfer, N.T.; Viswanathan, V.; Hunt, B.M.; Cohen-Karni, T. Electron Transport in Multidimensional Fuzzy Graphene Nanostructures. *Nano Lett.* **2019**, *19*, 5335–5339. [CrossRef]

27. Bao, L.; He, L.; Meyer, N.; Kou, X.; Zhang, P.; Chen, Z.G.; Fedorov, A.V.; Zou, J.; Riedemann, T.M.; Lograsso, T.A.; et al. Weak anti-localization and quantum oscillations of surface states in topological insulator Bi$_2$Se$_2$Te. *Sci. Rep.* **2012**, *2*, 726. [CrossRef]

28. Salvato, M.; Lucci, M.; Ottaviani, I.; Cirillo, M.; Orlanducci, S.; Toschi, F.; Terranova, M.L. Weak localization and dimensional crossover in carbon nanotube systems. *Eur. Phys. J. B* **2012**, *85*, 2–6. [CrossRef]

29. Takane, Y. Weak localization in multiwall carbon nanotubes in a perpendicular magnetic field. *J. Phys. Soc. Japan* **2006**, *75*, 044701. [CrossRef]

30. Ovsiienko, I.; Len, T.; Mirzoiev, I.; Beliayev, E.; Gnida, D.; Matzui, L.; Heraskevych, V. Low-temperature magnetoresistance of functionalized multiwall carbon nanotubes. *Fiz. Nizk. Temp.* **2023**, *49*, 17–33. [CrossRef]

31. Wolf, S.A.; Awschalom, D.D.; Buhrman, R.A.; Daughton, J.M.; Von Molnár, S.; Roukes, M.L.; Chtchelkanova, A.Y.; Treger, D.M. Spintronics: A spin-based electronics vision for the future. *Science* **2001**, *294*, 1488–1495. [CrossRef] [PubMed]

32. Pulizzi, F. Spintronics. *Nat. Mater.* **2012**, *11*, 367. [CrossRef] [PubMed]

33. Ahn, E.C. 2D materials for spintronic devices. *Npj 2D Mater. Appl.* **2020**, *4*, 17. [CrossRef]

34. Zeng, J.; Chen, K.Q. Magnetic configuration dependence of magnetoresistance in a Fe-porphyrin-like carbon nanotube spintronic device. *Appl. Phys. Lett.* **2014**, *104*, 033104. [CrossRef]

35. Andzane, J.; Katkov, M.V.; Buks, K.; Sarakovskis, A.; Smits, K.; Erts, D. Synthesis, magnetoresistance and thermoelectical properties of environmentally-stable n-type nitrogen-doped multiwalled carbon nanotubes. *Carbon Trends* **2023**, *13*, 100302. [CrossRef]

36. Andzane, J.; Buks, K.; Strakova, M.N.; Zubkins, M.; Bechelany, M.; Marnauza, M.; Baitimirova, M.; Erts, D. Structure and Doping Determined Thermoelectric Properties of Bi$_2$Se$_3$ Thin Films Deposited by Vapour-Solid Technique. *IEEE Trans. Nanotechnol.* **2019**, *18*, 948–954. [CrossRef]

37. Andzane, J.; Britala, L.; Kauranens, E.; Neciporenko, A.; Baitimirova, M.; Lara-Avila, S.; Kubatkin, S.; Bechelany, M.; Erts, D. Effect of graphene substrate type on formation of Bi$_2$Se$_3$ nanoplates. *Sci. Rep.* **2019**, *9*, 4791. [CrossRef] [PubMed]

38. Boschker, J.E.; Galves, L.A.; Flissikowski, T.; Lopes, J.M.J.; Riechert, H.; Calarco, R. Coincident-site lattice matching during van der Waals epitaxy. *Sci. Rep.* **2015**, *5*, 18079. [CrossRef]

39. Schaumann, J.; Loor, M.; Ünal, D.; Mudring, A.; Heimann, S.; Hagemann, U.; Schulz, S.; Maculewicz, F.; Schierning, G. Improving the zT value of thermoelectrics by nanostructuring: Tuning the nanoparticle morphology of Sb$_2$Te$_3$ by using ionic liquids. *Dalt. Trans.* **2017**, *46*, 656–668. [CrossRef]

40. Idriss, H. On the wrong assignment of the XPS O1s signal at 531–532 eV attributed to oxygen vacancies in photo- and electro-catalysts for water splitting and other materials applications. *Surf. Sci.* **2021**, *712*, 2–7. [CrossRef]

41. Meng, C.; Liu, C.; Fan, S. A promising approach to enhanced thermoelectric properties using carbon nanotube networks. *Adv. Mater.* **2010**, *22*, 535–539. [CrossRef] [PubMed]

42. Andzane, J.; Spalva, E.; Katkevics, J.; Bugovecka, L.; Kons, A.; Buks, K.; Erts, D. Thermoelectrical properties of bare and PDMS-encapsulated MWCNT-Sb$_2$Te$_3$ hybrid networks and their application in flexible heat-to-power conversion devices. *ACS Appl. Energy Mater.* **2023**, *6*, 10807–10816. [CrossRef]

43. Harutyunyan, S.R. Thickness-dependent magnetoresistance of Sb$_2$Te$_3$ nanoflakes and weak antilocalization effect. *J. Contemp. Phys.* **2015**, *50*, 282–287. [CrossRef]

44. Jash, A.; Kumar, A.; Ghosh, S.; Bharathi, A.; Banerjee, S.S. Imaging current distribution in a topological insulator Bi$_2$Se$_3$ in the presence of competing surface and bulk contributions to conductivity. *Sci. Rep.* **2021**, *11*, 7445. [CrossRef] [PubMed]

45. Kunakova, G.; Galletti, L.; Charpentier, S.; Andzane, J.; Erts, D.; Léonard, F.; Spataru, C.D.; Bauch, T.; Lombardi, F. Bulk-free topological insulator Bi$_2$Se$_3$ nanoribbons with magnetotransport signatures of Dirac surface states. *Nanoscale* **2018**, *10*, 19595–19602. [CrossRef] [PubMed]

46. Xue, J.; Huang, S.; Wang, J.Y.; Xu, H.Q. Mott variable-range hopping transport in a MoS$_2$ nanoflake. *RSC Adv.* **2019**, *9*, 17885–17890. [CrossRef]

47. Yu, D.; Wang, C.; Wehrenberg, B.L.; Guyot-Sionnest, P. Variable range hopping conduction in semiconductor nanocrystal solids. *Phys. Rev. Lett.* **2004**, *92*, 216802. [CrossRef]

48. Gupta, K.; Mukherjee, P.S.; Meikap, A.K.; Jana, P.C. Effect of samarium nanoparticles on the electrical transport properties of polyaniline. *Adv. Nat. Sci. Nanosci. Nanotechnol.* **2014**, *5*, 025003. [CrossRef]

49. Lähderanta, E.; Hajdeu-Chicarosh, E.; Guc, M.; Shakhov, M.A.; Zakharchuk, I.; Bodnar, I.V.; Arushanov, E.; Lisunov, K.G. Magnetotransport and conductivity mechanisms in Cu$_2$ZnSn$_x$Ge$_{1-x}$S$_4$ single crystals. *Sci. Rep.* **2018**, *8*, 17507. [CrossRef]

50. Spataru, C.D.; Léonard, F. Fermi-level pinning, charge transfer, and relaxation of spin-momentum locking at metal contacts to topological insulators. *Phys. Rev. B Condens. Matter Mater. Phys.* **2014**, *90*, 085115. [CrossRef]

51. Kumar, S.; Faraz, M.; Khare, N. Enhanced thermoelectric properties of Sb$_2$Te$_3$-graphene nanocomposite. *Mater. Res. Express* **2019**, *6*, 085079. [CrossRef]

52. Tanty, N.; Patra, A.; Maity, K.P.; Prasad, V. Tuning magnetoresistance and electrical resistivity by enhancing localization length in polyaniline and carbon nanotube composites. *Bull. Mater. Sci.* **2019**, *42*, 198. [CrossRef]

53. Ovsiienko, I.V.; Len, T.A.; Mirzoiev, I.G.; Beliayev, E.Y.; Gnida, D.; Matzui, L.Y.; Heraskevych, V.M. Low-temperature magnetore-sistance of multi-walled carbon nanotubes with perfect structure. *Low Temp. Phys.* **2022**, *48*, 89–98. [CrossRef]

54. Li, Q.; Li, Y.; Zhang, X.; Chikkannanavar, S.B.; Zhao, Y.; Dangelewicz, A.M.; Zheng, L.; Doorn, S.K.; Jia, Q.; Peterson, D.E.; et al. Structure-dependent electrical properties of carbon nanotube fibers. *Adv. Mater.* **2007**, *19*, 3358–3363. [CrossRef]

55. Antonova, I.V.; Nebogatikova, N.A.; Stepina, N.P.; Volodin, V.A.; Kirienko, V.V.; Rybin, M.G.; Obrazstova, E.D.; Golyashov, V.A.; Kokh, K.A.; Tereshchenko, O.E. Growth of Bi$_2$Se$_3$/graphene heterostructures with the room temperature high carrier mobility. *J. Mater. Sci.* **2021**, *56*, 9330–9343. [CrossRef]

56. Amaladass, E.P.; Devidas, T.R.; Sharma, S.; Sundar, C.S.; Mani, A.; Bharathi, A. Magneto-transport behaviour of Bi$_2$Se$_{3-x}$Te$_x$: Role of disorder. *J. Phys. Condens. Matter* **2016**, *28*, 075003. [CrossRef]

57. Kumar, Y.; Sultana, R.; Sharma, P.; Awana, V.P.S. Modeling of magneto-conductivity of bismuth selenide: A topological insulator. *SN Appl. Sci.* **2021**, *3*, 413. [CrossRef]

58. Lee, P.C.; Huang, Y.C.; Chien, C.H.; Chiu, F.Y.; Chen, Y.Y.; Harutyunyan, S.R. A comparative study of size-dependent magnetore-sistance and Hall resistance of Sb$_2$Te$_3$ nanoflakes. *Phys. B Condens. Matter* **2015**, *459*, 12–15. [CrossRef]

59. Jiang, Y.; Sun, Y.Y.; Chen, M.; Wang, Y.; Li, Z.; Song, C.; He, K.; Wang, L.; Chen, X.; Xue, Q.K.; et al. Fermi-level tuning of epitaxial Sb$_2$Te$_3$ thin films on graphene by regulating intrinsic defects and substrate transfer doping. *Phys. Rev. Lett.* **2012**, *108*, 066809. [CrossRef]

60. Bera, S.; Behera, P.; Mishra, A.K.; Krishnan, M.; Patidar, M.M.; Venkatesh, R.; Ganesan, V. Weak antilocalization in Sb$_2$Te$_3$ nano-crystalline topological insulator. *Appl. Surf. Sci.* **2019**, *496*, 143654. [CrossRef]

61. Alegria, L.D.; Schroer, M.D.; Chatterjee, A.; Poirier, G.R.; Pretko, M.; Patel, S.K.; Petta, J.R. Structural and electrical characterization of Bi$_2$Se$_3$ nanostructures grown by metal-organic chemical vapor deposition. *Nano Lett.* **2012**, *12*, 4711–4714. [CrossRef] [PubMed]

62. Lu, H.Z.; Shen, S.Q. Weak localization of bulk channels in topological insulator thin films. *Phys. Rev. B Condens. Matter Mater. Phys.* **2011**, *84*, 125138. [CrossRef]

63. Stepina, N.P.; Golyashov, V.A.; Nenashev, A.V.; Tereshchenko, O.E.; Kokh, K.A.; Kirienko, V.V.; Koptev, E.S.; Goldyreva, E.S.; Rybin, M.G.; Obraztsova, E.D.; et al. Weak antilocalization to weak localization transition in Bi$_2$Se$_3$ films on graphene. *Phys. E Low-Dimens. Syst. Nanostructures* **2022**, *135*, 2–6. [CrossRef]

64. Pang, H.-J.; Yu, H.; Li, W.-J.; Chen, L.-C.; Qiu, P.-F.; Peng, Q.; Chen, X.-J. Topological states of thermoelectric Yb-filled skutterudites. *Phys. Rev. B* **2023**, *107*, 125202. [CrossRef]